

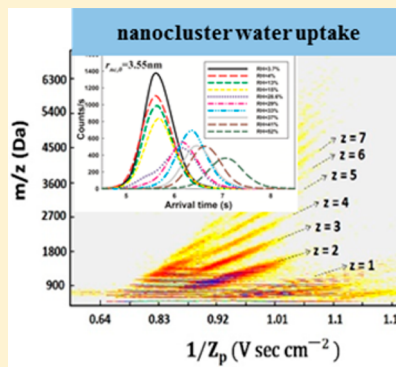
# IMS–MS and IMS–IMS Investigation of the Structure and Stability of Dimethylamine-Sulfuric Acid Nanoclusters

Hui Ouyang, Siqin He, Carlos Larriba-Andaluz, and Christopher J. Hogan, Jr.\*

Department of Mechanical Engineering, University of Minnesota, Minneapolis, Minnesota United States

## S Supporting Information

**ABSTRACT:** Recent studies of new particle formation events in the atmosphere suggest that nanoclusters (i.e., the species formed during the early stages of particle growth which are composed of  $10^1$ – $10^3$  molecules) may consist of amines and sulfuric acid. The physicochemical properties of sub-10 nm amine-sulfuric acid clusters are hence of interest. In this work, we measure the density, thermostability, and extent of water uptake of <8.5 nm effective diameter dimethylamine-sulfuric (DMAS) nanoclusters in the gas phase, produced via positive electrospray ionization. Specifically, we employ three systems to investigate DMAS properties: ion mobility spectrometry (IMS, with a parallel-plate differential mobility analyzer) is coupled with mass spectrometry to measure masses and collision cross sections for <100 kDa positively charged nanoclusters, two differential mobility analyzers in series (IMS–IMS) are used to examine thermostability, and finally a differential mobility analyzer coupled to an atmospheric pressure drift tube ion mobility spectrometer (also IMS–IMS) is used for water uptake measurements. IMS–MS measurements reveal that dry DMAS nanoclusters have densities of  $\sim 1567 \text{ kg/m}^3$  near 300 K, independent of the ratio of dimethylamine to sulfuric acid originally present in the electrospray solution. IMS–IMS thermostability studies reveal that partial pressures of DMAS nanoclusters are dependent upon the electrospray solution concentration ratio,  $R = [\text{H}_2\text{SO}_4]/[(\text{CH}_3)_2\text{NH}]$ . Extrapolating measurements, we estimate that dry DMAS nanoclusters have surface vapor pressures of order  $10^{-4}$  Pa near 300 K, with the surface vapor pressure increasing with increasing values of  $R$  through most of the probed concentration range. This suggests that nanocluster surface vapor pressures are substantially enhanced by capillarity effects (the Kelvin effect). Meanwhile, IMS–IMS water uptake measurements show clearly that DMAS nanoclusters uptake water at relative humidities beyond 10% near 300 K, and that larger clusters uptake water to a larger extent. In total, our results suggest that dry DMAS nanoclusters (in the 5–8.5 nm size range in diameter) would not be stable under ambient conditions; however, DMAS nanoclusters would likely be hydrated in the ambient (in some cases above 20% water by mass), which could serve to reduce surface vapor pressures and stabilize them from dissociation.



## INTRODUCTION

There is strong evidence that new particle formation events in the ambient atmosphere lead to the formation of clusters composed of amines in combination with sulfuric acid;<sup>1–3</sup> though amines have lower atmospheric concentrations than ammonia,<sup>4,5</sup> because of their stronger basicity than ammonia,<sup>6</sup> amine-sulfuric acid clusters are more stable in ambient conditions than are ammonium sulfate/ammonium bisulfate clusters. In particular, dimethylamine molecules [ $(\text{CH}_3)_2\text{NH}$ ] in combination with sulfuric acid molecules ( $\text{H}_2\text{SO}_4$ ) form condensed phase species (dimethylamine-sulfuric acid clusters, DMAS, which are combinations of dimethylammonium sulfate and/or dimethylammonium bisulfate), which have been found to be more stable than their methylamine- and trimethylamine-sulfuric acid cluster counterparts.<sup>6,7</sup> As a result, DMAS are highly likely to be the seeds for nanoparticle growth in many new particle formation events in the atmosphere.<sup>1,8–11</sup>

Of considerable interest are thus the physicochemical properties of DMAS in the 1–10 nm size range. Such entities are typically composed of  $10^1$ – $10^3$  molecules and are

henceforth referred to as nanoclusters here. Though in the initial stages of new particle formation clusters composed of a smaller number of molecules (< $10^1$ ) form,<sup>6,12</sup> these smaller clusters must grow into nanoclusters and it is nanocluster properties (namely their density, thermostability, and capacity to uptake water) which govern subsequent growth to larger nanoparticles [i.e., to eventually act as CCN (cloud condensation nuclei)]. The nanoclusters must not dissociate under atmospherically relevant conditions and further must be able to grow by vapor uptake (via condensation). When input into models of condensational particle growth in the ambient atmosphere,<sup>13,14</sup> nanocluster physicochemical properties will have a direct influence on the model output particle growth rate. Of concern for nanoclusters is that although modeling them as spheres is likely acceptable, the properties of nanoclusters can, and presumably do, deviate from bulk

Received: December 18, 2014

Revised: February 16, 2015

Published: February 18, 2015

properties as well as from the properties of larger nano- to submicrometer particles, with such deviations not necessarily predictable from classically derived theories (though such theories are used almost universally in modeling nanocluster growth<sup>13</sup>). For example, the capillarity model (i.e., the Kelvin effect)<sup>15,16</sup> leads to the prediction that nanoclusters are much less thermostable than larger species of the same chemical composition and have substantially higher vapor pressures than their bulk counterparts. While qualitatively this is true, the capillarity model is based upon a bulk definition of surface tension; simulations<sup>17</sup> show that for pure phase nanoclusters whose radii are  $\leq 7$  van der Waals radii, quantitatively the capillarity model leads to extremely inaccurate vapor pressure predictions. Additional deviations from the capillarity model are to be expected for the vapor pressures of multicomponent nanoclusters, such as DMAS. Furthermore, size dependencies/ deviations from bulk behavior are also expected and have been observed for the density<sup>18</sup> and extent of water uptake of nanoclusters.<sup>19–21</sup>

DMAS nanoclusters and larger nanoparticles have been studied experimentally and theoretically by several different approaches. An overview of the properties of amines and studies of atmospheric amine chemistry was recently provided by Qiu and Zhang.<sup>22</sup> Specifically for DMAS particles, Qiu and Zhang also measured the thermostability, density, and extent of water vapor uptake for particles in the 80 to 240 nm size (diameter) range.<sup>7</sup> Ab initio calculations have been performed by several research groups to study the formation of neutral or charged DMAS clusters with or without water molecules.<sup>9,12,23–26</sup> However, experimental measurements in the nanocluster size range are lacking (beyond measurements of clusters composed of  $\leq 10$  sulfuric acids, above a size of  $\sim 1.1$  nm in diameter). In this study, we thus focus on measurements of the properties of DMAS nanoclusters in the size (effective diameter) range of 2–8.5 nm, produced in a laboratory setting via electrospray ionization (ESI). Of specific interest are the density, thermostability, and extent of water uptake by such nanoclusters, properties which are amenable to laboratory investigation. Three unique measurement systems are employed for measurements of these properties, which are described in detail in the subsequent sections: for density measurement ion mobility spectrometry–mass spectrometry with a high-resolution differential mobility analyzer coupled to a mass spectrometer is applied;<sup>18,27–29</sup> for thermostability a tandem differential mobility analyzer system<sup>30,31</sup> using modest-to-high resolution differential mobility analyzers<sup>32</sup> is utilized; and for heterogeneous water uptake experiments, a differential mobility analyzer-drift tube mobility analysis system is applied.<sup>21,33</sup> The overarching goal of this work is to better understand what the properties of DMAS nanoclusters would be under atmospherically relevant conditions.

## ■ EXPERIMENTAL METHODS

**Materials.** As a source of gas phase DMAS nanoclusters, we used ESI of methanol based solutions, which, upon methanol evaporation, yielded nanoclusters. Solutions were prepared by adding sulfuric acid (99.999%) and dimethylamine (40 wt % in H<sub>2</sub>O) to HPLC-grade methanol. All chemicals were purchased from Sigma-Aldrich (Saint Louis, MO). Variable molar concentrations of sulfuric acid and dimethylamine were used, which are denoted as [H<sub>2</sub>SO<sub>4</sub>] and [(CH<sub>3</sub>)<sub>2</sub>NH] respectively. Seven molar concentration ratios,  $R = [\text{H}_2\text{SO}_4]/[(\text{CH}_3)_2\text{NH}]$  were employed, specifically,  $R = 10, 5, 4, 3, 2, 1$ , and 0.5. These

solutions were used for nanocluster generation with all three employed measurement systems.

For ESI, a 40  $\mu\text{m}$  i.d. silica capillary (360  $\mu\text{m}$  o.d., Polymicro Technologies, Phoenix, AZ) was used, as was used previously in cluster ion generation experiments.<sup>18,27</sup> An applied pressure was used to drive the solution through the capillary, while a positive voltage was applied directly to the solution to run the electrospray in a cone-jet mode,<sup>34</sup> which was observed to be stable visually with a magnifying lens. DMAS nanoclusters with either single or multiple excess positive charges were formed via ESI; for IMS–MS measurement, the ESI voltage was floated over the outer electrode of the parallel-plate differential mobility analyzer employed, and no charge reduction scheme was employed prior to measurements. Conversely, for tandem differential mobility analyzer experiments and differential mobility-analyzer-drift tube experiments a 0.5 mCi Po-210 source was used to reduce the charge level of nanoclusters; after charge reduction most nanoclusters were neutral and those that were observed were singly charged.<sup>35,36</sup>

### Differential Mobility Analysis–Mass Spectrometry.

Differential mobility analysis-mass spectrometry,<sup>29</sup> a form of ion mobility spectrometry–mass spectrometry (IMS–MS)<sup>37,38</sup> was used for measurement of the collision cross sections of mass-identified nanoclusters in air. From these measurements, nanocluster densities can be inferred.<sup>39,40</sup> The parallel plate differential mobility analyzer (model p5 SEADM, Boecillio, Spain, with a resolving power in mobility near 60) and QSTAR XL time-of-flight mass spectrometer (Applied Biosystems, Framingham, MA) combination has been described in detail previously<sup>18,27,29</sup> and was operated in a similar manner to these prior works. Briefly, to specify the mobilities of the nanoclusters which can traverse the differential mobility analyzer, a potential difference was generated between the two electrodes by applying a voltage on the outer electrode. Singly and multiply charged nanoclusters were drawn into the classification region electrostatically, with the inlet operated in counterflow mode ( $\sim 0.1 \text{ L min}^{-1}$  of counterflow). High purity air (Air Gas, Ultra ZeroG1 ppm, St. Paul, MN) was used as the sheath flow gas, and the sheath flow was operated in recirculating mode using a vacuum blower (Domel Inc., Železniki, Slovenia) with the sheath gas temperature in the measurement zone near 303 K and close to atmospheric pressure.  $\sim 0.2 \text{ L min}^{-1}$  was drawn into the mass spectrometer inlet (at the outlet of the classification region of the mobility analyzer), to continuously supply air for the outlet and for the counterflow a mass flow controller (MKS instruments, Andover, MA) was set at 0.3 L min<sup>-1</sup>.

To collect combined mass-mobility spectra, a potential difference of 1000–4000 V was applied in steps of 10 V, and mass spectra were collected at each voltage for an accumulation time of 2 s. For mass spectra measurements, the quadrupole mass filters were operated in radiofrequency-only mode, and the time-of-flight section was employed. Between the mobility analyzer outlet and the first quadrupole of the mass spectrometer, there are several applied declustering and focusing potential differences; all of these differences were set to minimal values to mitigate the dissociation of nanoclusters in the mass spectrometer inlet (i.e., to reduce collision induced dissociation). Prior IMS–MS measurements where the IMS was operated at atmospheric pressure have revealed that in the inlets (where ions/nanoclusters are exposed to high pressure drop as well as strong electric fields) of mass spectrometers

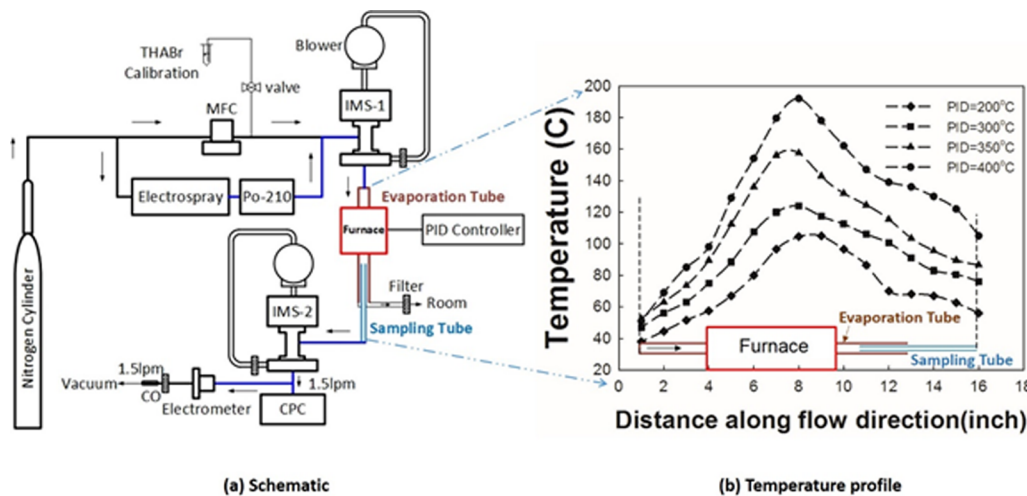


**Figure 1.** (a) A depiction of the tandem differential mobility analyzer system employed in thermostability experiments (IMS: differential mobility analyzer; CPC: condensation particle counter; Po-210: bipolar ion source). (b) The temperature profiles measured axially in the microfurnace chamber. The position of the furnace heating chamber and the sampling tube are also depicted.

with atmospheric pressure ionization, collision-induced dissociation of nanoclusters is commonplace.<sup>18,28,41,42</sup>

As in prior studies using high sheath flow rate (in excess of 100 L min<sup>-1</sup>) parallel-plate differential mobility analyzers, we did not measure the sheath flow rate directly. Instead, as differential mobility analyzers are linear spectrometers (i.e., the applied voltage is linearly proportional to the inverse mobility of the selected ions/nanoclusters), we employed a single-point calibration technique. Prior to all experiments, we measured the electrical mobility of the tetraheptylammonium<sup>+</sup> (THA<sup>+</sup>) ion, produced via ESI of a tetraheptylammonium bromide-methanol solution. The mobility of this ion ( $Z_{\text{THA}}$ ), measured by Ude and Fernández de la Mora<sup>43</sup> at 293 K was used to determine mobility of observed nanoclusters ( $Z_{\text{nc}}$ ) through the relationship:  $Z_{\text{nc}} = (V_{\text{THA}}/V_{\text{nc}}) \times Z_{\text{THA}}$ , where  $V_{\text{THA}}$  is the applied voltage at which the THA<sup>+</sup> ion was maximally transmitted, and  $V_{\text{nc}}$  is the voltage at which the nanocluster in question was maximally transmitted. Neglecting the influence of the ion-induced dipole potential, for calibration,  $Z_{\text{THA}}$  was adjusted from Ude and Fernandez de la Mora's measured value because of the difference in temperatures used in measurement here and in their work (303 K vs 293 K, leading to a 1.6% shift in the mobility).

**IMS–IMS Investigation of Thermostability.** Tandem differential mobility analysis, a form of IMS–IMS,<sup>44</sup> has been successfully used in thermostability studies for over two decades.<sup>30,45,46</sup> We applied a similar measurement principle here, using two differential mobility analyzers of modest-to-high resolving power (typically above 20) for measurements. The tandem differential mobility analysis system employed is depicted in Figure 1a. In it, industrial-grade dry nitrogen was used as a carrier gas, and DMAS nanoclusters were generated as described by an electrospray, with subsequent charge reduction in a Po-210 source. A flow of dry nitrogen was subsequently mixed with the generated nanocluster flow, with a 3.87 L min<sup>-1</sup> of aerosol flow entering the first differential mobility analyzer (labeled as IMS-1 in Figure 1a).

Both differential mobility analyzers were cylindrical 1/2 mini models (Nanoengineering Corp., Boca Raton, FL), the design of which is described by Fernandez de la Mora and Kozlowski.<sup>32</sup> In both, a negative voltage was applied to the inner electrode where the aerosol exit slit is located, while the

outer electrode is grounded. Positively charged nanoclusters were hence selected and measured. The sheath flows were operated in a recirculating mode with Domel Inc. vacuum blowers, and again, the THA<sup>+</sup> ion was used for calibration. The first differential mobility analyzer was operated at a fixed voltage to transmit nanoclusters of a specific mobility (and hence radius, as nearly all charged nanoclusters were singly charged). To evaluate thermostability, a microfurnace (UltraCoil Robust Radiator, Micropyretics Heaters International Inc., Cincinnati, OH) was placed between the two differential mobility analyzers, and nanoclusters transmitted through the first differential mobility analyzer were sent through the microfurnace via a 12 in. long sintered silicon carbide round tube (the evaporation tube) with 1/2 in. o.d. and 3/8 in. i.d. (Ortech Inc., Sacramento, CA). Nanocluster evaporation occurred in the heated zone of the microfurnace, which was a 1.5 in. diameter and 3.5 in. length cylindrical chamber. Two insulating caps with the thicknesses of 0.75 in. were used to seal the heating chamber, and a PID controller was connected to a thermocouple embedded in the heated zone. The temperature profile was varied in the furnace by adjusting PID controller values. Four specific temperatures were set with the PID controller: 200, 300, 350, and 400 °C. However, because the flow within the silicon carbide tube was laminar, and heating was nonuniform, an axial temperature profile was developed in the silicon carbide tube (i.e., the PID controller set temperature was not the temperature in the evaporation tube). Temperature profiles along the length of the evaporation tube were hence measured for all experiments and are displayed in Figure 1b. The temperature increased first and then decreased, with the highest temperature appearing at an axial location two-thirds downstream in the microfurnace (because of convective heat transfer). After the evaporation tube, an alumina sampling tube, which only sampled the center streamlines of the evaporation tube (3 L min<sup>-1</sup> sampled), transmitted particles exiting the microfurnace to the second differential mobility analyzer (IMS-2). The second differential mobility analyzer was operated with a stepping applied voltage in the 0 to 4000 V range, with a step rate of 10 V s<sup>-1</sup>, in order to determine to what extent the selected nanoclusters evaporated when passing through the microfurnace. The flow at the second differential mobility analyzer outlet was split, with half entering a condensation

particle counter (CPC, TSI model 3776, Shoreview, MN) and the other half entering a custom-made Faraday cage electrometer. The CPC was used primarily for thermostability measurements (nanocluster detection), while the electrometer was used for  $\text{THA}^+$  detection and, hence, mobility calibration (which was repeated at all PID controller set temperatures).

**IMS–IMS Investigation of Water Uptake.** While tandem differential mobility analyzers can be used to examine the sorption of vapor molecules to nanoparticles, maintaining high sheath flow rates at constant vapor concentrations (i.e., constant relative humidities) can be difficult. As an alternative, our group has recently developed a drift tube ion mobility spectrometer (DT-IMS, described in detail previously<sup>33</sup>) which can be uniquely coupled to a CPC for nanoparticle and nanocluster measurements. When using the DT-IMS in tandem with a differential mobility analyzer upstream, by controlling the relative humidity of its counterflow ( $\sim 0.2 \text{ L min}^{-1}$ ), shifts in nanocluster mobilities brought about by vapor uptake can be directly observed. Following the experimental setup described by Oberreit et al.,<sup>21</sup> ESI generated and charge reduced DMAS nanoclusters were first passed through a 1/2 mini differential mobility analyzer, which was again operated at a constant applied voltage to isolate nanoclusters of a specific mobility. The selected nanoclusters then entered the DT-IMS, which was operated with clean air as the counterflow and humidified with a custom flow rate controlled nebulizer-heater system. The relative humidity in the DT-IMS was calculated from dew point and temperature measurements with a hygrometer (General Eastern Hygro M4, Fairfield, CT) and a K type thermocouple, respectively.

Without any applied voltage, all nanoclusters entering the DT-IMS were immediately swept out of the inlet by the counterflow. However, upon timed application of a voltage (3 kV in this study) at the inlet, a near-linear electric field forms axially, driving positively charged nanoclusters down the tube at a speed equal to the difference between their electrophoretic velocities and the counterflow velocity. Therefore, nanocluster arrival times at the CPC placed downstream of the DT-IMS are solely a function of nanocluster mobilities. Specifically, the inverse mobility ( $Z_{nc}^{-1}$ ) of a nanocluster is linked to its arrival time ( $t_a$ ) as measured by a CPC via the equation:  $Z_{nc}^{-1} = at_a + b$ , where  $a$  and  $b$  are constants dependent upon the delay time in CPC detection, the counterflow velocity, the applied voltage, and the drift tube geometry. To minimize signal broadening, a fast response CPC (WCPC, model 3786, TSI, Shoreview, MN) was employed in all measurements.

The differential mobility analyzer-DTMS system enabled the investigation of water vapor uptake by nanoclusters via observation of uptake facilitated shifts in inverse mobilities, which was directly inferred from shifts in mobility classified nanocluster arrival time distributions. Again, we used ESI generated  $\text{THA}^+$  to calibrate the 1/2 mini differential mobility analyzer, and subsequently, mobility classified particles were used to determine the values of  $a$  and  $b$  in DT-IMS calibration. For uptake experiments, five voltages were applied to the 1/2 mini differential mobility analyzer (5 nanocluster sizes) and arrival time distributions were measured correspondingly for 10 different relative humidity settings in the 3%–52% range.

## RESULTS AND DISCUSSION

**Nanocluster Collision Cross Sections and Inferred Densities.** IMS–MS measurements directly lead to mass-mobility spectra, in which measured signal intensity is displayed

as a function of both mass-to-charge ratio ( $m/z$ ) and inverse mobility ( $1/Z_{nc}$ ), which is directly proportional to the applied voltage in the differential mobility analyzer. In IMS–MS experiments, five solutions with different molar ratios,  $R = [\text{H}_2\text{SO}_4]/[(\text{CH}_3)_2\text{NH}]$  were used to generate DMAS nanoclusters, and each gave rise to their own mass-mobility spectra. Such data can be represented via contour plots; a contour plot for  $R = 1$  is displayed in Figure 2. In it, signal intensity for each

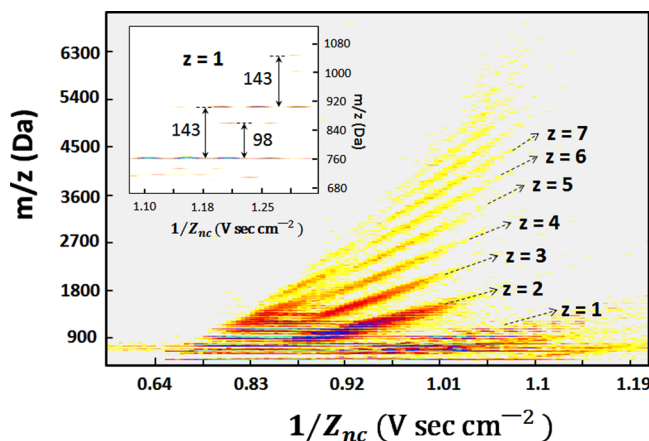


**Figure 2.** A mass-mobility contour plot inferred from IMS–MS measurement of multiply charged DMAS nanoclusters, with measured signal intensity expressed via color intensity on a logarithmic scale, with blue the most intense and yellow the least intense. Bands of ions of different charge states are labeled, from  $z = 1$  to 7.

ion is displayed via a logarithmic color scale, with blue denoting the most intense signal and yellow denoting the faintest signal above a prescribed threshold. Signal intensities were mass averaged over 0.3 Da. In the displayed contour plot, short line segments appear; each line segment denotes an ion of a specific  $m/z$  and  $1/Z_{nc}$ , and the width of the line represents the resolution of the ion mobility spectrometer. As discussed in detail previously, line segments for electrospray generated nanoclusters are grouped into charge-state specific bands.<sup>18,27,47–49</sup> Bands for seven charge states ( $z = 1$  to 7) are labeled in the figure. For several of the singly charged nanoclusters, a zoomed-in plot is inserted in Figure 2.

Apparent in this plot is that nanoclusters differ in  $m/z$  from one another by either 98 or 143 Da. For doubly charged species, the mass differences observed are half of these values; together these indicate that nanoclusters are composed predominantly of  $[(\text{CH}_3)_2\text{NH}\cdot\text{H}_2\text{SO}_4]$  and  $[\text{H}_2\text{SO}_4]$  base units. In several instances, nanoclusters of the same  $m/z$  ratio but varying inverse mobility appear. Such line segments are attributable to neutral ion-pair ( $[(\text{CH}_3)_2\text{NH}\cdot\text{H}_2\text{SO}_4]$  or  $[\text{H}_2\text{SO}_4]$ ) evaporation in the inlet of the mass spectrometer (after mobility classification).<sup>28</sup> Charge loss in the mass spectrometer inlet (in particular for  $z = 2$  nanoclusters) additionally complicates spectra, giving rise to wider line segments which appear at neither the  $m/z$  nor the inverse mobility of the parent nanoclusters.<sup>27</sup> Fortunately, neutral evaporation and charge loss are minimal for most multiply charged nanoclusters, hence the  $m/z$  and  $1/Z_{nc}$  values, as well as  $z$ , are readily determined from measurements for these nanoclusters. Subsequently, collision cross sections (CCSs,  $\Omega$ ) can be calculated for nanoclusters from mass-mobility data:

$$\Omega = \left( \frac{\pi m_{\text{red}}}{8kT} \right)^{0.5} \frac{3ze}{4\rho_{\text{gas}} Z_{\text{nc}}} \quad (1a)$$

where  $m_{\text{red}}$  is the reduced mass of the nanocluster–gas molecule pair (approximated as the gas molecule mass for all nanoclusters, 28.8 Da),  $k$  is Boltzmann's constant,  $T$  is temperature,  $e$  is the elementary charge, and  $\rho_{\text{gas}}$  is the bath gas mass density. In examining smaller clusters, structural analysis via IMS is best accomplished via comparison of measured CCSs to predictions based upon gas molecule scattering calculations;<sup>18,39,41,50–52</sup> the asphericity of such entities, combined with the non-negligible influence of the ion-induced dipole potential (for measurements in air) and some ambiguity in the manner in which gas molecules impinge and are re-emitted from clusters surfaces (i.e., diffuse versus specular) often prohibits the use of simple relationships to link the CCS to physical structure. However, nanoclusters are sufficiently large, such that they can be approximated as spheres.<sup>47</sup> For spherical entities in diatomic gases,<sup>41</sup> considering the free-molecular limit of the Stokes-Millikan equation<sup>39,40,50,53</sup> as well as the influence of the polarization potential between gas molecule and charged nanocluster,<sup>54</sup> the following relationship can be applied to link the CCS to a nanocluster's radius,  $r_{\text{nc}}$ :

$$\Omega = \xi \times \pi \times (r_{\text{nc}} + r_{\text{gas}})^2 \times L \quad (1b)$$

where  $r_{\text{gas}}$  is the effective gas molecule radius (1.5 Å for air near 300 K<sup>47</sup>),  $\xi$  is a dimensionless momentum scattering coefficient, found to be  $\approx 1.36$  in many instances and taken to be so here (though exception have been observed<sup>18</sup>), and  $L$  is a dimensionless polarization correction factor (a correction factor of the ion induced-dipole potential), the calculation of which is described in detail by Larriba-Andaluz and Hogan:<sup>39</sup>

$$L = \left[ 1 + \phi_e \left( \frac{1}{3.1} + \frac{1}{\xi} \left( \frac{1}{16} + \frac{4}{33} \phi_e \right) \right) \right] \text{ if } \phi_e \leq 1 \quad (1c)$$

$$L = \left[ 1 + \phi_e \left( \frac{1}{4} - \frac{2.3}{1000} \phi_e + \frac{1}{\xi} \left( \frac{9}{56} - \frac{6.8}{1000} \phi_e \right) \right) \right] \text{ if } \phi_e > 1 \quad (1d)$$

where  $\phi_e = U_{\text{pol}}/kT$  (potential energy to thermal energy ratio), and  $U_{\text{pol}} = -\alpha z^2 e^2 / [8\pi \epsilon_0 (r_{\text{nc}} + r_{\text{gas}})^4]$ , with  $\epsilon_0$  the permittivity of free space,  $\epsilon$  the dielectric constant of the background gas, and  $\alpha$  the polarizability of the background gas molecules ( $\sim 1.7$  Å<sup>3</sup> in air).

For each nanocluster measured, we infer  $r_{\text{nc}}$  with eqs (1–4). Additionally, in Figure 3, the masses of all multiply charged nanoclusters are plotted as functions of  $\Omega^{3/2}$ ; for these clusters, polarization influences (though considered in  $r_{\text{nc}}$  inference) are small, and additionally  $r_{\text{nc}}$  is considerably larger than  $r_{\text{gas}}$ . Therefore,  $\Omega^{3/2}$  scales approximately with nanocluster volume, and the observed linear relationship between nanocluster mass and  $\Omega^{3/2}$  suggests that the measured nanoclusters are of a constant density, which is found relatively independent of the sulfuric acid to dimethylamine concentration ratio  $R$  in ESI solutions. As discussed in prior studies,<sup>47</sup> high-resolution ion mobility spectrometry of mass-identified ions enables density inference to within several percent; however, density inference alone does enable quantification of nanocluster internal structure or surface structure changes which may be brought about by changing  $R$  ratios. Via linear regression with all data in

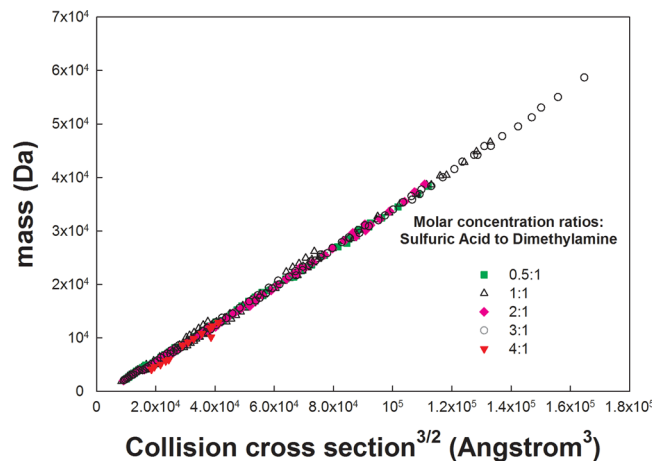


**Figure 3.** Measured mass of nanoclusters as a function of their collision cross sections to the 3/2 power, which is approximately proportional to nanocluster volume. Different symbols represent different molar concentration ratios of initial solution used in ESI solutions.

Figure 3, we infer a density,  $\rho_{\text{DMAS}} = m_{\text{nc}} / (4/3\pi r_{\text{nc}}^3)$ , of 1567 kg m<sup>-3</sup>. Although this value is slightly higher than the 97 nm diameter particle DMAS density reported by Qiu and Zhang<sup>7</sup> (1408 kg m<sup>-3</sup>), it is bounded by bulk densities of dimethylamine (670 kg m<sup>-3</sup>) and sulfuric acid (1840 kg m<sup>-3</sup>) and further increases in density for nanoclusters (due to capillarity effects, provided charged clusters are not Coulombically stretched)<sup>47</sup> are expected.

**Nanocluster Thermostability.** For tandem differential mobility analysis experiments, we additionally use eq 1b to infer nanocluster radii,  $r_{\text{nc}}$  for the nanoclusters transmitted by both the first and second differential mobility analyzers, respectively. For all results,  $L = 1$  was assumed, as for the singly charged nanoclusters examined in these experiments, polarization influences are negligible. Measurements result in plots of measured signal intensity (CPC signal) as a function of  $r_{\text{nc}}$  for each selected  $r_{\text{nc},0}$  by the first differential mobility analyzer and each set temperature profile in the furnace. Such plots are displayed in Figure 4 for  $r_{\text{nc},0} = 3.00, 3.30, 3.66$ , and 3.95 nm with 4 different PID settings. Evidenced in this figure, in all instances, as the PID set temperature was increased, (1) the absolute detected signal decreased, (2) distributions became noticeably broader and asymmetric, and (3) peaks in distributions shifted to smaller inferred radii. The first observation is attributable to thermophoretic deposition in the furnace, while the second and third are attributable to evaporation (monomer dissociation) of nanoclusters at elevated temperatures, with broadening presumably arising because of variations in the temperature–time history by transmitted nanoclusters (spatial effects). Although attempts were made to minimize such broadening and spatial influences on the evaporation process by sampling along the evaporation tube centerline only, such effects are difficult to completely mitigate<sup>31</sup> in a system for sub 10 nm charged entities.

While we nonetheless proceed to infer surface vapor pressures for nanoclusters ( $P_{\text{nc}}$ ) from these measurements, we caution that the absolute values obtained have not been corrected considering a detailed analysis of the temperature profile in the evaporation tube and the nanocluster trajectories (i.e., an averaging approaching is taken), and further, the analysis approach itself utilizes several approximations.

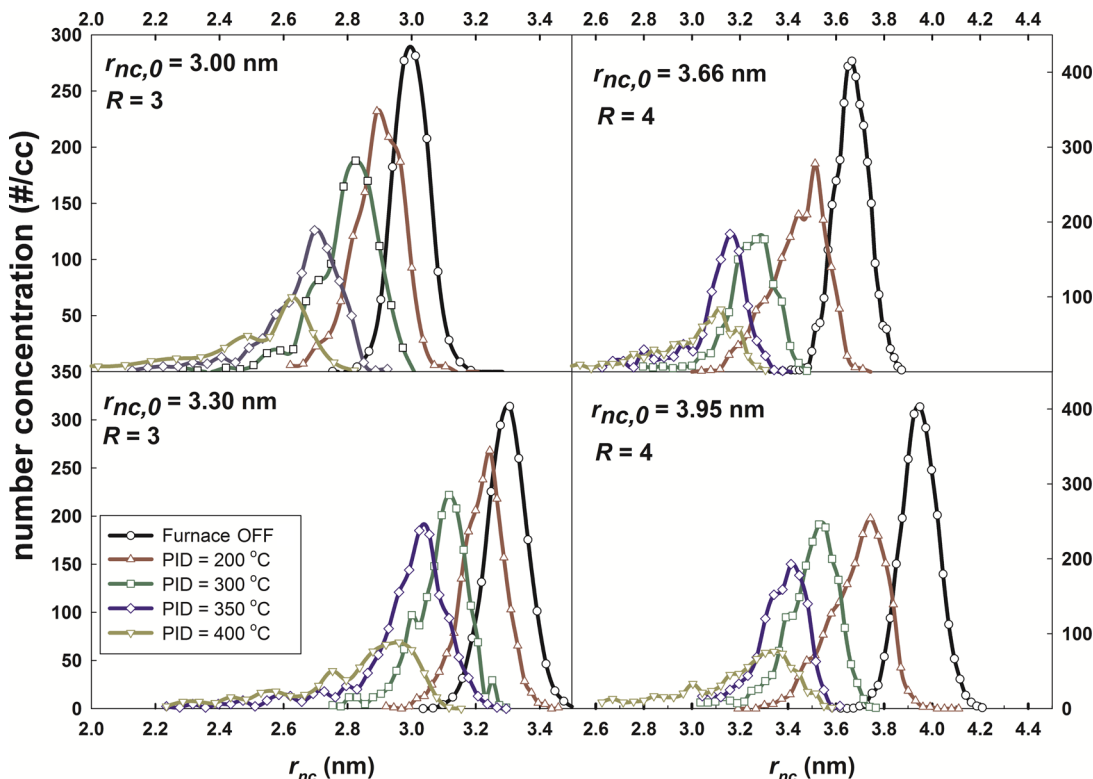


**Figure 4.** Nanocluster number concentrations, as measured by a CPC, measured as a function of  $r_{nc}$  based on the second differential mobility analyzer settings in tandem differential mobility experiments for different temperatures (distinguished by PID setting) and for four initial radii.

However, we will only focus on estimating the surface vapor pressures to within an order of magnitude, which such approximations should not mitigate.

To analyze tandem differential mobility analyzer data, we determine the peak  $r_{nc}$  values for each measured distribution and assume that all of these nanoclusters were transmitted through the evaporation tube with near identical residence times ( $t$ ). The number of vapor molecules evaporating from the surface of a single nanocluster per unit time (the evaporation rate,  $dN/dt$ , in units of molecules per second) is given by the equation:

$$\frac{dN}{dt} = -\beta n_{v,nc} \quad (2a)$$

where  $n_{v,nc}$  is the vapor molecule number concentration on the surface of a nanocluster, and  $\beta$  is the collision kernel/collision rate coefficient, which for nanoclusters in the ballistic regime can be approximated as  $(8kT/\pi m_v)^{1/2} \times \pi r_{nc}^2$ , where  $(8kT/\pi m_v)^{1/2}$  is the mean thermal speed of the evaporating vapor molecules, and  $m_v$  is the mass of vapor (assumed to be 98 Da, the mass of sulfuric acid, for reasons elaborated upon later on).

The surface concentration of vapor molecules, in turn, can be converted to a nanocluster surface vapor pressure via the relationship  $n_v = P_{nc}/kT$ . With the number of vapor molecules in a nanocluster given by  $\rho V_{nc}/m_v$ , where  $V_{nc}$  is the nanocluster volume [assuming they are spheres  $V_{nc} = (4/3)\pi r_{nc}^3$ ] and  $\rho$  the density (measured in IMS-MS experiments), it then follows that  $dN/dt = (\rho/m_v)(dV_{nc}/dt)$ . This relationship coupled with the assumption that the density and vapor molecule mass are nanocluster size invariant leads to

$$\frac{dV_{nc}(t)}{dt} = -\sqrt{\frac{8kT(t)}{\pi m_v}} \cdot \pi r_{nc}^2 \cdot \frac{P_{nc}(T, r_{nc})}{kT(t)} \cdot \frac{m_v}{\rho} \quad (2b)$$

In eq 2b, the nanocluster volume and the temperature are denoted as functions of time, while the nanocluster vapor pressure is denoted as a function of temperature and the nanocluster radius. Measurements provide the initial and final nanocluster volume, respectively, and the temperature-time relationship for the centerline of the evaporation tube was measured as discussed previously (at 16 discrete axial distances). These two pieces of information, combined with eq 2b, enable inference of  $P_{nc}(T, r_{nc})$ . Isolating  $dV_{nc}$  on the left-hand side of eq 2b and integrating over the residence time  $t$  in the furnace leads to

$$\begin{aligned} \frac{4}{3}\pi(r_{nc,0}^3 - r_{nc,f}^3) &= \Delta V \\ &\approx \frac{r_{nc,0}^2}{\rho} \cdot \sqrt{\frac{8\pi m_v}{k}} \cdot \int_0^t \frac{P_{nc}(T, r_{nc,0})}{\sqrt{T(t)}} dt \end{aligned} \quad (2c)$$

where  $r_{nc,f}$  is the final peak radius of the transmitted nanoclusters and  $\Delta V$  is the volume change due to evaporation. In integrating 2b, for simplicity, we assume that  $r_{nc}^2 \approx r_{nc,0}^2$  (i.e., the projected area of an evaporating nanocluster did not change substantially during experiments). In addition, vapor pressures inferred are assumed to apply for clusters of radius  $r_{nc,0}$ .

To subsequently determine  $P_{nc}(T)$ , for each  $r_{nc,0}$  we used the fitting function:

$$P_{nc}(T) = \exp\left(A^2 - \frac{B^2}{T} - \frac{C^2}{T^{1.5}} - \frac{D^2}{T^{0.5}}\right) \quad (2d)$$

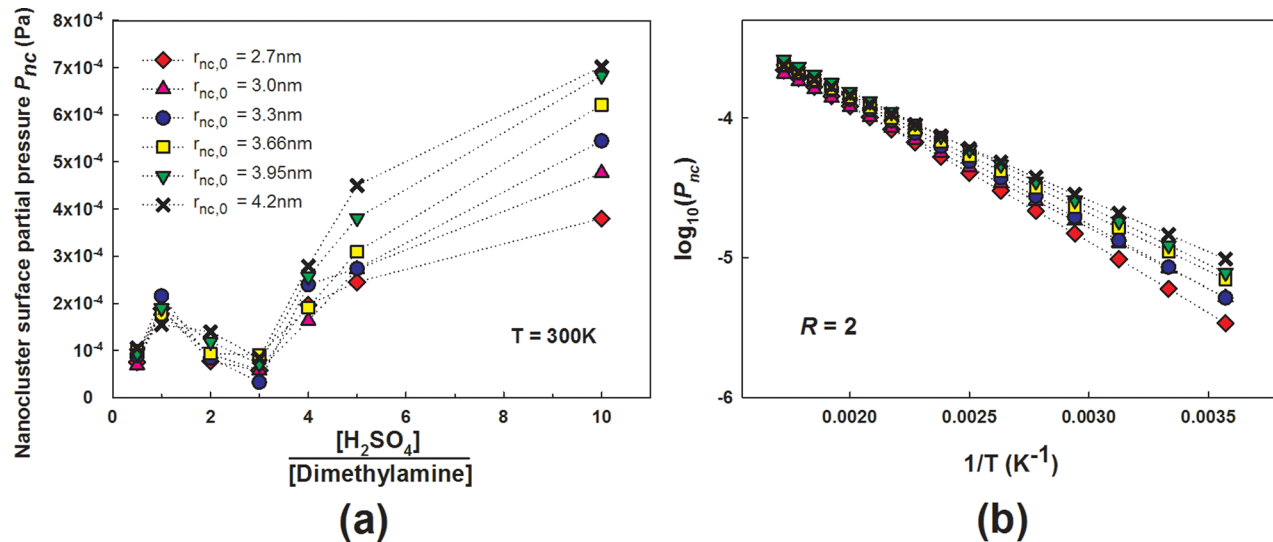


**Figure 5.** (a) Extrapolated surface vapor pressures,  $P_{nc}$ , as a function of  $R = [\text{H}_2\text{SO}_4]/[(\text{CH}_3)_2\text{NH}]$ . (b)  $\log_{10}(P_{nc})$  inferred from experiments, based on fitting eq 2d to experimental results, as a function of  $1/T$ . Different symbols represent different initial particle radii:  $\blacklozenge$  (2.68 nm),  $\blacktriangle$  (3.05 nm),  $\bullet$  (3.38 nm),  $\blacksquare$  (3.68 nm),  $\blacktriangledown$  (3.97 nm) and  $\times$  (4.23 nm).

where  $A$ ,  $B$ ,  $C$ , and  $D$  are fitting coefficients, the temperature  $T$  is in Kelvin, and the resulting pressure is in Pascals. This function is similar in construction to the Antoine equation<sup>55</sup> or Riedel equation,<sup>56</sup> though it is simply used because of its flexibility in fitting our results and is not derived from thermodynamic relationships (i.e., the third and fourth terms are ad-hoc corrections, introduced only to provide flexibility in fitting results). With substitution of eq 2d into eq 2c, combined with the trapezoidal rule for integration, eq 2c can be rearranged to give:

$$\Delta V_i \cdot \frac{\rho}{\pi r_{nc,0}^2} \cdot \sqrt{\frac{\pi k}{8m_v}} \approx \sum_{j=1}^{15} \left\{ \left( \frac{\exp\left(A^2 - \frac{B^2}{T_{j,i}} - \frac{C^2}{T_{j,i}^{1.5}} - \frac{D^2}{T_{j,i}^{0.5}}\right)}{T_{j,i}^{0.5}} \right. \right. \\ \left. \left. + \frac{\exp\left(A^2 - \frac{B^2}{T_{j+1,i}} - \frac{C^2}{T_{j+1,i}^{1.5}} - \frac{D^2}{T_{j+1,i}^{0.5}}\right)}{T_{j+1,i}^{0.5}} \right) / 2 \cdot \delta t \right\} \quad (2e)$$

where  $i = 1, 2, 3$ , and  $4$  denotes the four PID set values (200, 300, 350, and 400 °C, respectively),  $T_{j,i}$  denotes the temperature measured at location  $j$  for PID setting  $i$ , and  $\delta t = t/15$ . To find the “best-fit” values of  $A$ ,  $B$ ,  $C$ , and  $D$ , for which the left-hand side and right-hand side of eq 2e are approximately equal for all PID settings, we use the solver add-in of Microsoft Excel (version 2010). A global error is defined as  $e_G = \sum_{i=1}^4 [1 - (a_i/b_i)]^2$ , where  $a_i$  and  $b_i$  are left-hand and right-hand sides of eq 2e, respectively. Local errors were also similarly calculated as  $e_i = |1 - (a_i/b_i)|$ . Using initial guesses of  $A = 1$ ,  $B = 10$ ,  $C = 100$ , and  $D = 10$ , under all circumstances, the solver minimizes  $e_G$  while keeping all  $e_i$  less than 15% as a constraint, with the exception of the PID setting of 200 °C, for which no constraint is placed. Different initial guess values led to a negligible change in the resulting  $P_{nc}$  values, and this fitting procedure is applied for six separate initial sizes, and seven values of  $R$ , hence 42 separate coefficient sets.

Table S1 of the Supporting Information contains lists of inferred values  $A$ ,  $B$ ,  $C$ , and  $D$  for all measured  $r_{nc,0}$  and  $R$  values. Upon the basis of these values, in Figure 5a we plot the values of  $P_{nc}$  extrapolated to 300 K as a function of  $R$ , and in Figure 5b we plot  $P_{nc}$  [quantified by  $\log_{10}(P_{nc})$ ] as a function of inverse temperature. Nanocluster vapor pressures near 300 K are on the order of  $10^{-4}$ – $10^{-3}$  Pa for nearly all circumstances. These values are substantially higher (by multiple orders of magnitude) than ammonium sulfate surface vapor pressures inferred by Marti et al.,<sup>57</sup> for larger nanoparticles (50–300 nm diameters) under dry conditions and even larger than surface vapor pressure of larger DMAS particles inferred by Lavi et al.,<sup>58</sup> who found that DMAS particles have lower vapor pressures than ammonium sulfate submicrometer particles. However, our surface vapor pressure extrapolations are only an order of magnitude larger than the vapor pressure of 50–300 nm sulfuric acid–water nanoparticles (76% sulfuric acid by mass) estimated by Marti et al. (of order  $10^{-5}$  Pa). At atmospheric pressure, our extrapolated vapor pressures correspond to nanocluster surface vapor concentrations in the ppbv (parts per billion by volume) range. Ambient sulfuric acid concentrations are typically in the pptv (parts per trillion by volume range),<sup>3,59</sup> and dimethylamine concentrations are expected to be in a similar, subppbv range.<sup>59</sup> Despite the approximations employed in analysis as well as the extrapolation used to 300 K, our error in vapor pressure estimation is presumably not several orders of magnitude, and our measurements strongly suggest the surface vapor pressures of dry DMAS nanoclusters are higher than ambient vapor pressures for their constituents. We also note the vapor pressures inferred are sensitive to the choice of  $m_v$  but not to an extent which alters the order of  $P_{nc}$  values. Such high-surface vapor pressures suggest that it is excess sulfuric acid evaporating from dry clusters, and likely arise because of a Kelvin model-like behavior for nanoclusters; the Kelvin effect<sup>53</sup> predicts that the vapor pressure at the surface of a nanocluster will increase over the bulk value by a factor of  $p(2\gamma m_v/\rho k T r_{nc})$ , where  $\gamma$  is the effective surface energy density of the nanocluster (i.e., the surface tension, expected to high for ionically bonded systems). High surface energy densities can thus lead surface vapor

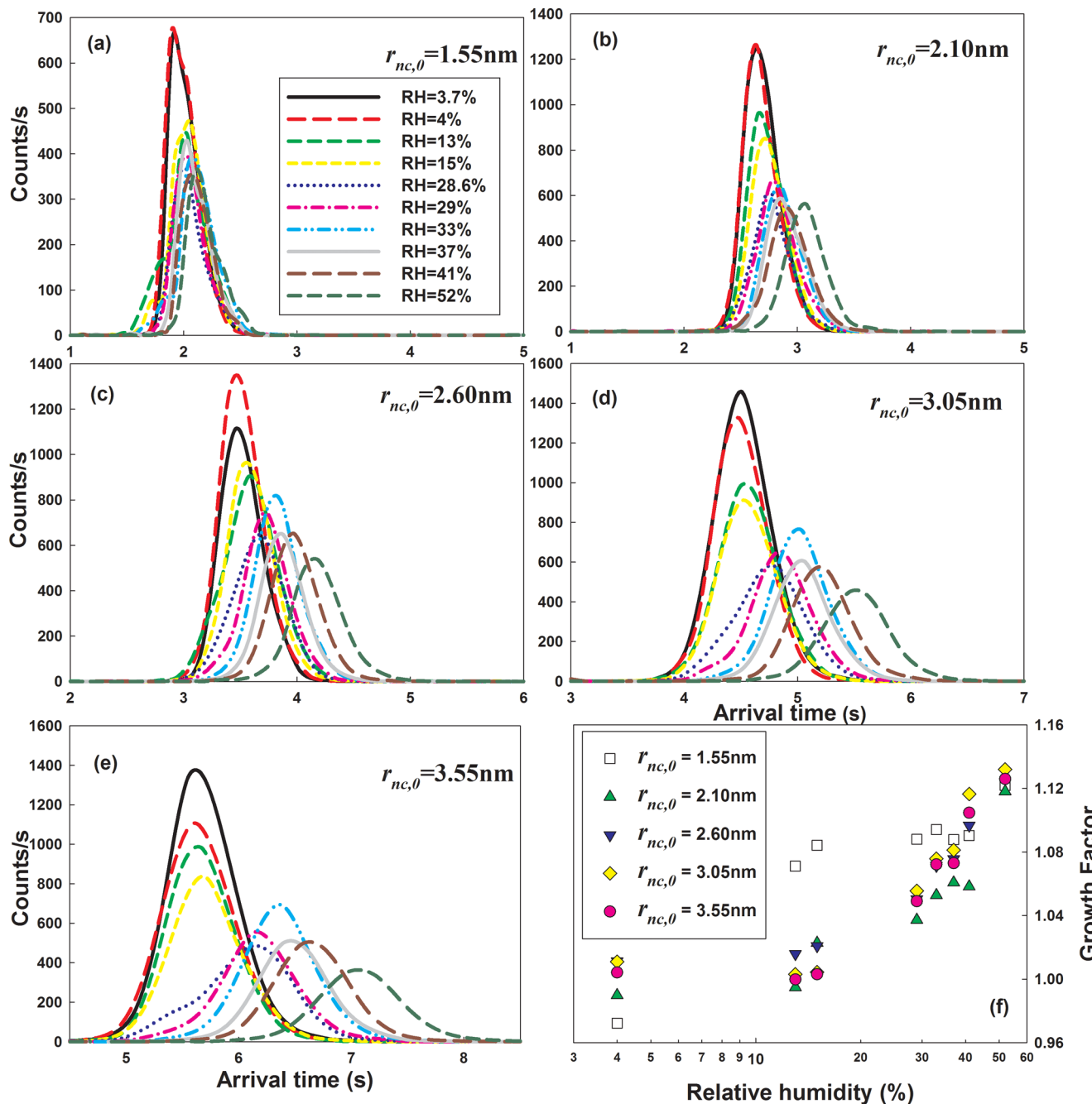


**Figure 6.** (a–e) Arrival time distributions for five separate dry nanocluster radii and with 10 separate relative humidities (RHs) in the drift tube ion mobility spectrometer. (f) The inferred growth factor for nanoclusters of five different dry radii as a function of relative humidity.

pressures enhanced by several orders of magnitude over bulk values (hence our measurements are in-line with the vapor pressure estimations of Marti et al.<sup>57</sup> for larger, nearly dry sulfuric acid particles), creating a barrier to dry nanocluster growth. The observation of high surface vapor pressures for nanoclusters is further supported by attempts to analyze  $R = 0$  (pure dimethylamine) and  $R = \infty$  (pure sulfuric acid) nanoclusters; in these circumstances, nanoclusters evaporate almost completely at room temperature prior to transmission through ion mobility spectrometers, such that we could not detect clusters from pure dimethylamine or pure sulfuric acid solutions. Interestingly, a clear nanocluster size dependency of the vapor pressure (increasing vapor pressure with decreasing size) is not observed in the nanocluster size range examined, in

fact at large  $R$  values an increase in  $P_{nc}$  with increasing radius is observed. This is likely because of compounding influences of size-dependent chemical composition (from the nanocluster formation process in these experiments) and direct size influences on the surface vapor pressure and because the size range examined itself was relatively narrow. An increase in  $P_{nc}$  is additionally observed with increasing  $R$ , and hence increasing sulfuric acid content was further evidence that sulfuric acid is the major evaporating species from DMAS nanoclusters.

**Nanocluster Water Vapor Uptake.** While our thermostability measurements suggest that dry DMAS nanoclusters ( $r_{nc} = 2.5\text{--}4$  nm) may not grow by condensation purely of sulfuric acid and dimethylamine under ambient conditions, our results do not preclude DMAS constituents from being the

primary species involved in the earlier stages of new particle formation (as smaller clusters have been found stable).<sup>2,6</sup> Further, as pure, dry DMAS nanoclusters were examined, our results do not preclude other species from condensing onto DMAS and reducing surface vapor pressures, thus stabilizing them. One such species that could stabilize nanoclusters is water vapor. It has been shown (again by Marti et al.<sup>57</sup>) that the sorption of water vapor by particles composed of sulfuric acid or ammonium sulfate decreases by orders of magnitude, even in instances where the extent of sorption leads to particles which are still primarily sulfuric acid or ammonium sulfate. We therefore use differential mobility analyzer-DT-IMS experiments<sup>21,33</sup> to examine the extent of water uptake by DMAS nanoclusters as a function of nanocluster dry radius. Arrival time distributions, in which CPC inferred nanocluster counts per second are plotted as functions of time required for nanoclusters to arrive at the CPC, are shown in Figure 6 (panels a–e) for  $R = 2$  nm nanoclusters with 5 selected initial sizes and at 10 separate relative humidities. Evident is the shift in spectra to longer arrival times with increasing relative humidity for all initial nanocluster radii. As a negative control experiment, electrospray-generated cesium iodide nanoclusters<sup>18</sup> were also measured (results not shown), and no change in the arrival time distributions was observed for these nanoclusters at any relative humidity in the range examined. The shift in arrival time brought about by increasing relative humidity is thus indicative of a decrease in the electrical mobility of DMAS nanoclusters (i.e., water vapor did not change the DT-IMS calibration curve), which, in turn, is indicative of water uptake by these nanoclusters. Water uptake by larger alkylammonium salts has been observed in prior studies;<sup>7,58</sup> thus, our observation of water uptake by nanoclusters under subsaturated conditions is not surprising. To quantify the extent of uptake, following prior work,<sup>60,61</sup> we calculated the growth factor (GF) for all nanoclusters as a function of relative humidity (RH), via the equation:

$$GF = \frac{(r_{nc} + r_{gas})_{RH}}{(r_{nc} + r_{gas})_{RH=3.7\%}} \quad (3)$$

We include the gas molecule radius in GF calculations for consistency with Oberreit et al.,<sup>21</sup> and  $r_{nc}$  in eq 3 is inferred using eq 1 as well as the DT-IMS calibration curve with the peak in arrival time distributions. The baseline relative humidity of 3.7% was the lowest humidity achievable in experiments. Growth factors as functions of relative humidity are shown in Figure 6f. For nanoclusters of all measured initial radii, growth factors increase with increasing relative humidity but remain in the 0.98–1.13 range. With the exception of the smallest nanoclusters examined ( $r_{nc} = 1.55$  nm), we find that for a given relative humidity, growth factors increase slightly with initial nanocluster radius, suggesting that larger nanocluster uptake proportionally more water vapor. For example, at a relative humidity of 29%, measurements suggest that nanoclusters with initial radii of 2.1 nm uptake ~174 water vapor molecules on average (based on the change in volume) and correspondingly are ~8.2% water by mass, while initially 3.05 nm radius nanoclusters uptake ~659 water molecules and are 9.9% water by mass. At the highest relative humidity examined, measurements suggest that initially 3.05 nm nanoclusters uptake ~1860 water molecules and are ~23.7% water by mass. Overall, the evidence for water uptake under conditions resembling ambient air is clear in these IMS–IMS experiments, hence such

nanoclusters should be modeled as partially hydrated species. However, as has been found in quantum mechanical calculations for smaller DMAS clusters,<sup>24</sup> the extent of hydration is insufficient to permit modeling nanoclusters as aqueous droplets containing dissolved cations and anions. Future work, both experimental and computational, will be necessary to better resolve the internal structures of such hydrated nanoclusters.

## CONCLUSIONS

A series ion mobility spectrometry based measured have been performed to study the physicochemical properties of dimethylamine-sulfuric acid (DMAS) nanoclusters in the effective diameter range of <8.5 nm ( $2^*r_{nc}$ ). Independent of the ratio of sulfuric acid to dimethylamine in electrospray solutions used in cluster generation from IMS–MS measurements, we find that the average density of dry DMAS nanoclusters is ~1567 kg m<sup>-3</sup>, which is inferred from IMS–MS results through the polarization-corrected free molecular limit of the Stokes–Millikan equation.<sup>39</sup> This value is slightly (~10%) higher than has been reported for larger DMAS nanoparticles and submicrometer particles,<sup>7,58</sup> suggesting that the nanoclusters studied here may have contained excess sulfuric acid (note that for the multiply charged nanoclusters in IMS–MS analysis, adducts prevent clear chemical identification from mass measurements alone). Thermostability measurement inferred vapor pressures for DMAS nanoclusters suggest that their surface vapor pressures near 300 K are orders of magnitude higher than the vapor pressures of sulfuric acid or dimethylamine in ambient air<sup>59,62</sup> and are an order of magnitude higher than the vapor pressure found for larger sulfuric acid nanoparticles.<sup>57</sup> Measurements hence suggest that it is excess sulfuric acid which dissociates from nanoclusters (as the vapor pressure increases with increasing sulfuric acid vapor pressure), and capillarity effects (i.e., the Kelvin effect) enhance DMAS nanocluster vapor pressure to an extent where dry nanoclusters would not necessarily be stable in the ambient. However, IMS–IMS measurements of water uptake show that DMAS nanoclusters uptake water and are hydrated at relative humidities beyond 10% (near 300 K). Such water uptake likely serves to stabilize nanoclusters (reducing surface vapor pressures). The measurements reported here are for an important size range between that of clusters and nanoparticles. These latter two size ranges are studied much more frequently than nanoclusters; mass spectrometry lends itself to cluster analysis,<sup>2,3</sup> while differential mobility analysis (and various forms of aerosol mass spectrometry<sup>63,64</sup>) are applicable to larger nanoparticles and submicrometer particles. Unfortunately nanocluster concentrations are often too low to detect via cluster mass spectrometry or by aerosol mass spectrometry in the ambient. Nonetheless, as the properties of species in this size range ultimately affect particle growth in the ambient (i.e., all particles originating in new particle formation events were once nanoclusters), it is important to develop techniques amenable to nanocluster characterization. The tandem techniques utilized here may find continued utility in nanocluster analysis.

## ASSOCIATED CONTENT

### S Supporting Information

A list of A, B, C, and D values, used in inference of nanocluster vapor pressures (as per eq 2d), is provided in Table S1. This

material is available free of charge via the Internet at <http://pubs.acs.org>.

## AUTHOR INFORMATION

### Corresponding Author

\*E-mail: hogan108@umn.edu.

### Notes

The authors declare no competing financial interest.

## ACKNOWLEDGMENTS

This work was supported by National Science Foundation Grant CHE-1011810. H.O. acknowledges support from a University of Minnesota Doctoral Dissertation Fellowship. C.L.A. acknowledges support from a Ramon Areces Foundation Fellowship.

## REFERENCES

- (1) Paasonen, P.; Olenius, T.; Kupiainen, O.; Kurten, T.; Petaja, T.; Birmili, W.; Hamed, A.; Hu, M.; Huey, L. G.; Plass-Duelmer, C.; et al. On the Formation of Sulphuric Acid - Amine Clusters in Varying Atmospheric Conditions and its Influence on Atmospheric New Particle Formation. *Atmos. Chem. Phys.* **2012**, *12*, 9113–9133.
- (2) Kurten, A.; Jokinen, T.; Simon, M.; Sipila, M.; Sarnela, N.; Junninen, H.; Adamov, A.; Almeida, J.; Amorim, A.; Bianchi, F.; et al. Neutral Molecular Cluster Formation of Sulfuric Acid-Dimethylamine Observed in Real Time Under Atmospheric Conditions. *Proc. Natl. Acad. Sci. U.S.A.* **2014**, *111*, 15019–15024.
- (3) Zhao, J.; Smith, J. N.; Eisele, F. L.; Chen, M.; Kuang, C.; McMurry, P. H. Observation of Neutral Sulfuric Acid-Amine Containing Clusters in Laboratory and Ambient Measurements. *Atmos. Chem. Phys.* **2011**, *11*, 10823–10836.
- (4) Sorooshian, A.; Murphy, S. N.; Hersey, S.; Gates, H.; Padro, L. T.; Nenes, A.; Brechtel, F. J.; Jonsson, H.; Flagan, R. C.; Seinfeld, J. H. Comprehensive Airborne Characterization of Aerosol from a Major Bovine Source. *Atmos. Chem. Phys.* **2008**, *8*, 5489–5520.
- (5) Ge, X. L.; Wexler, A. S.; Clegg, S. L. Atmospheric Amines: Part I. A Review. *Atmos. Environ.* **2011**, *45*, 524–546.
- (6) Jen, C. N.; McMurry, P. H.; Hanson, D. R. Stabilization of Sulfuric Acid Dimers by Ammonia, Methylamine, Dimethylamine, and Trimethylamine. *J. Geophys. Res.: Atmos.* **2014**, *119*, 7502–7514.
- (7) Qiu, C.; Zhang, R. Y. Physiochemical Properties of Alkylaminium Sulfates: Hygroscopicity, Thermostability, and Density. *Environ. Sci. Technol.* **2012**, *46*, 4474–4480.
- (8) Kurten, T.; Loukonen, V.; Vehkamaki, H.; Kulmala, M. Amines are Likely to Enhance Neutral and Ion-Induced Sulfuric Acid-Water Nucleation in the Atmosphere more Effectively than Ammonia. *Atmos. Chem. Phys.* **2008**, *8*, 4095–4103.
- (9) Loukonen, V.; Kurten, T.; Ortega, I. K.; Vehkamaki, H.; Padua, A. H.; Sellegri, K.; Kulmala, M. Enhancing Effect of Dimethylamine in Sulfuric Acid Nucleation in the Presence of Water: A Computational Study. *Atmos. Chem. Phys.* **2010**, *10*, 4961–4974.
- (10) Bzdek, B. R.; Ridge, D. P.; Johnston, M. V. Amine Reactivity with Charged Sulfuric Acid Clusters. *Atmos. Chem. Phys.* **2011**, *11*, 8735–8743.
- (11) Petaja, T.; Sipila, M.; Paasonen, P.; Nieminen, T.; Kurten, T.; Ortega, I. K.; Stratmann, F.; Vehkamaki, H.; Berndt, T.; Kulmala, M. Experimental Observation of Strongly Bound Dimers of Sulfuric Acid: Application to Nucleation in the Atmosphere. *Phys. Rev. Lett.* **2011**, *106*, 228302.
- (12) Henschel, H.; Navarro, J. C. A.; Yli-Juuti, T.; Kupiainen-Määttä, O.; Olenius, T.; Ortega, I. K.; Clegg, S. L.; Kurtén, T.; Riipinen, I.; Vehkamäki, H. Hydration of Atmospherically Relevant Molecular Clusters: Computational Chemistry and Classical Thermodynamics. *J. Phys. Chem. A* **2014**, *118*, 2599–2611.
- (13) Kulmala, M.; Kerminen, V. M.; Anttila, T.; Laaksonen, A.; O'Dowd, C. D. Organic Aerosol Formation via Sulphate Cluster Activation. *J. Geophys. Res.: Atmos.* **2004**, *109*, D04205.
- (14) Donahue, N. M.; Trump, E. R.; Pierce, J. R.; Riipinen, I. Theoretical Constraints on Pure Vapor-Pressure Driven Condensation of Organics to Ultrafine Particles. *Geophys. Res. Lett.* **2011**, *38*, L16801.
- (15) Thomson, S. W. On the Equilibrium of Vapour at a Curved Surface of Liquid. *Philos. Mag. Lett.* **1871**, *4*, 448–452.
- (16) Zhang, K. M.; Wexler, A. S. A Hypothesis for Growth of Fresh Atmospheric Nuclei. *J. Geophys. Res.: Atmos.* **2002**, *107*, D214577.
- (17) Thompson, S. M.; Gubbins, K. E.; Walton, J. P. R. B.; Chantry, R. A. R.; Rowlinson, J. S. A Molecular Dynamics Study of Liquid Drops. *J. Chem. Phys.* **1984**, *81*, 530–542.
- (18) Ouyang, H.; Larriba-Andaluz, C.; Oberreit, D. R.; Hogan, C. J. The Collision Cross Sections of Iodide Salt Cluster Ions in Air via Differential Mobility Analysis-Mass Spectrometry. *J. Am. Soc. Mass Spectrom.* **2013**, *24*, 1833–1847.
- (19) Park, K.; Kim, J. S.; Miller, A. L. A Study on Effects of Size and Structure on Hygroscopicity of Nanoparticles using a Tandem Differential Mobility Analyzer and TEM. *J. Nanopart. Res.* **2009**, *11*, 175–183.
- (20) Biskos, G.; Malinowski, A.; Russell, L. M.; Buseck, P. R.; Martin, S. T. Nanosize Effect on the Deliquescence and the Efflorescence of Sodium Chloride Particles. *Aerosol Sci. Technol.* **2006**, *40*, 97–106.
- (21) Oberreit, D. R.; McMurry, P. H.; Hogan, C. J. Analysis of Heterogeneous Uptake by Nanoparticles via Differential Mobility Analysis-Drift Tube Ion Mobility Spectrometry. *Phys. Chem. Chem. Phys.* **2014**, *16*, 6968–6979.
- (22) Qiu, C.; Zhang, R. Y. Multiphase Chemistry of Atmospheric Amines. *Phys. Chem. Chem. Phys.* **2013**, *15*, 5738–5752.
- (23) DePalma, J. W.; Bzdek, B. R.; Doren, D. J.; Johnston, M. V. Structure and Energetics of Nanometer Size Clusters of Sulfuric Acid with Ammonia and Dimethylamine. *J. Phys. Chem. A* **2012**, *116*, 1030–1040.
- (24) DePalma, J. W.; Doren, D. J.; Johnston, M. V. Formation and Growth of Molecular Clusters Containing Sulfuric Acid, Water, Ammonia, and Dimethylamine. *J. Phys. Chem. A* **2014**, *118*, 5464–5473.
- (25) Ortega, I. K.; Olenius, T.; Kupiainen-Määttä, O.; Loukonen, V.; Kurtén, T.; Vehkamäki, H. Electrical Charging Changes the Composition of Sulfuric Acid-Ammonia/Dimethylamine Clusters. *Atmos. Chem. Phys.* **2014**, *14*, 7995–8007.
- (26) Ortega, I. K.; Kupiainen, O.; Kurten, T.; Olenius, T.; Wilkman, O.; McGrath, M. J.; Loukonen, V.; Vehkamaki, H. From Quantum Chemical Formation Free Energies to Evaporation Rates. *Atmos. Chem. Phys.* **2012**, *12*, 225–235.
- (27) Hogan, C. J.; Fernandez de la Mora, J. Tandem Ion Mobility-Mass Spectrometry (IMS-MS) Study of Ion Evaporation from Ionic Liquid-Acetonitrile Nanodrops. *Phys. Chem. Chem. Phys.* **2009**, *11*, 8079–8090.
- (28) Hogan, C. J.; Fernandez de la Mora, J. Ion-Pair Evaporation from Ionic Liquid Clusters. *J. Am. Soc. Mass Spectrom.* **2010**, *21*, 1382–1386.
- (29) Rus, J.; Moro, D.; Sillero, J. A.; Royuela, J.; Casado, A.; Estevez-Molinero, F.; Fernandez de la Mora, J. IMS-MS Studies Based on Coupling a Differential Mobility Analyzer (DMA) to Commercial API-MS Systems. *Int. J. Mass Spectrom.* **2010**, *298*, 30–40.
- (30) Rader, D. J.; McMurry, P. H. Application of the Tandem Differential Mobility Analyzer to Studies of Droplet Growth or Evaporation. *J. Aerosol Sci.* **1986**, *17*, 771–787.
- (31) Villani, P.; Picard, D.; Michaud, V.; Laj, P.; Wiedensohler, A. Design and Validation of a Volatility Hygroscopic Tandem Differential Mobility Analyzer (VH-TDMA) to Characterize the Relationships between the Thermal and Hygroscopic Properties of Atmospheric Aerosol Particles. *Aerosol Sci. Technol.* **2008**, *42*, 729–741.
- (32) Fernández de la Mora, J.; Kozlowski, J. Hand-Held Differential Mobility Analyzers of High Resolution for 1–30 nm Particles: Design and Fabrication Considerations. *J. Aerosol Sci.* **2013**, *57*, 45–53.
- (33) Oberreit, D. R.; McMurry, P. H.; Hogan, C. J. Mobility Analysis of 2 to 11 nm Aerosol Particles with an Aspirating Drift Tube Ion Mobility Spectrometer. *Aerosol Sci. Technol.* **2014**, *48*, 108–118.

- (34) Cloupeau, M.; Prunet-Foch, B. Electrostatic Spraying of Liquids in Cone-Jet Mode. *J. Electrost.* **1989**, *22*, 135–159.
- (35) Chen, D. R.; Pui, D. Y. H.; Kaufman, S. L. Electrospraying of Conducting Liquids for Monodisperse Aerosol Generation in the 4 nm to 1.8 mm Diameter Range. *J. Aerosol Sci.* **1995**, *26*, 963–977.
- (36) Scalf, M.; Westphall, M. S.; Smith, L. M. Charge Reduction Electrospray Mass Spectrometry. *Anal. Chem.* **2000**, *72*, 52–60.
- (37) Guharay, S. K.; Dwivedi, P.; Hill, H. H. Ion Mobility Spectrometry: Ion Source Development and Applications in Physical and Biological Sciences. *IEEE Trans. Plasma Sci.* **2008**, *36*, 1458–1470.
- (38) Kanu, A. B.; Dwivedi, P.; Tam, M.; Matz, L.; Hill, H. H. Ion Mobility-Mass Spectrometry. *J. Mass Spectrom.* **2008**, *43*, 1–22.
- (39) Larriba, C.; Hogan, C. J. Ion Mobilities in Diatomic Gases: Measurement versus Prediction with Non-Specular Scattering Models. *J. Phys. Chem. A* **2013**, *117*, 3887–3901.
- (40) Ku, B. K.; Fernandez de la Mora, J. Relation between Electrical Mobility, Mass, and Size for Nanodrops 1–6.5 nm in Diameter in Air. *Aerosol Sci. Technol.* **2009**, *43*, 241–249.
- (41) Larriba-Andaluz, C.; Fernandez-Garcia, J.; Hogan, C. J.; Clemmer, D. E. Gas Molecule Scattering & Ion Mobility Measurements for Organic Macro-ions in He versus N<sub>2</sub> Environments. *Phys. Chem. Chem. Phys.* **2014**, submitted.
- (42) Larriba, C.; Fernandez de la Mora, J.; Clemmer, D. E. Electrospray Ionization Mechanisms for Large Polyethylene Glycol Chains Studied Through Tandem Ion Mobility Spectrometry. *J. Am. Soc. Mass Spectrom.* **2014**, *25*, 1332–1345.
- (43) Ude, S.; Fernández de la Mora, J. Molecular Monodisperse Mobility and Mass Standards from Electrosprays of Tetra-Alkyl Ammonium Halides. *J. Aerosol Sci.* **2005**, *36*, 1224–1237.
- (44) Koeniger, S. L.; Merenbloom, S. I.; Valentine, S. J.; Jarrold, M. F.; Udseth, H. R.; Smith, R. D.; Clemmer, D. E. An IMS–IMS Analogue of MS-MS. *Anal. Chem.* **2006**, *78*, 4161–4174.
- (45) Rader, D. J.; McMurry, P. H.; Smith, S. Evaporation Rates of Monodisperse Organic Aerosols in the 0.02–Mu-M-Diameter to 0.2–Mu-M-Diameter Range. *Aerosol Sci. Technol.* **1987**, *6*, 247–260.
- (46) Park, K.; Dutcher, D.; Emery, M.; Pagels, J.; Sakurai, H.; Scheckman, J.; Qian, S.; Stolzenburg, M. R.; Wang, X.; Yang, J.; et al. Tandem Measurements of Aerosol Properties: A Review of Mobility Techniques with Extensions. *Aerosol Sci. Technol.* **2008**, *42*, 801–816.
- (47) Larriba, C.; Hogan, C. J.; Attoui, M.; Borrajo, R.; Fernandez-Garcia, J.; Fernandez de la Mora, J. The Mobility-Volume Relationship below 3.0 nm Examined by Tandem Mobility-Mass Measurement. *Aerosol Sci. Technol.* **2011**, *45*, 453–467.
- (48) Fernández-García, J.; Fernández de la Mora, J. Measuring the Effect of Ion-Induced Drift-Gas Polarization on the Electrical Mobilities of Multiply-Charged Ionic Liquid Nanodrops in Air. *J. Am. Soc. Mass Spectrom.* **2013**, *24*, 1872–1889.
- (49) Fernández-García, J.; Fernández de la Mora, J. Electrical Mobilities of Multiply Charged Ionic-Liquid Nanodrops in Air and Carbon Dioxide over a Wide Temperature Range: Influence of Ion-Induced Dipole Interactions. *Phys. Chem. Chem. Phys.* **2014**, *16*, 20500–20513.
- (50) Larriba, C.; Hogan, C. J. Free Molecular Collision Cross Section Calculation Methods for Nanoparticles and Complex Ions with Energy Accommodation. *J. Comput. Phys.* **2013**, *251*, 344–363.
- (51) Kumar, A.; Kang, S.; Larriba-Andaluz, C.; Ouyang, H.; Hogan, C. J.; Sankaran, R. M. Ligand-free Ni Nanocluster Formation at Atmospheric Pressure via Rapid Quenching in a Microplasma Process. *Nanotechnology* **2014**, *25*, 385601.
- (52) Larriba-Andaluz, C.; Hogan, C. J. Collision Cross Section Calculations for Polyatomic Ions Considering Rotating Diatomic/Linear Gas Molecules. *J. Chem. Phys.* **2014**, *141*, 194107.
- (53) Friedlander, S. K. *Smoke, Dust, and Haze*; Oxford University Press: New York, NY, 2000.
- (54) Tammet, H. Size and Mobility of Nanometer Particles, Clusters and Ions. *J. Aerosol Sci.* **1995**, *26*, 459–475.
- (55) Antoine, C. Tensions des Vapeurs; Nouvelle Relation Entre les Tensions et les Températures. *C. R. Séances Acad. Sci.* **1888**, *107*, 681–684 778–780, 836–837.
- (56) Vetere, A. The Riedel Equation. *Ind. Eng. Chem. Res.* **1991**, *30*, 2487–2492.
- (57) Marti, J. J.; Jefferson, A.; Cai, X. P.; Richert, C.; McMurry, P. H.; Eisele, F. H<sub>2</sub>SO<sub>4</sub> Vapor Pressure of Sulfuric Acid and Ammonium Sulfate Solutions. *J. Geophys. Res.: Atmos.* **1997**, *102*, 3725–3735.
- (58) Lavi, A.; Bluvstein, N.; Segre, E.; Segev, L.; Flores, M.; Rudich, Y. Thermochemical, Cloud Condensation Nucleation Ability, and Optical Properties of Alkyl Aminium Sulfate Aerosols. *J. Phys. Chem. C* **2013**, *117*, 22412–22421.
- (59) Almeida, J.; Schobesberger, S.; Kurten, A.; Ortega, I. K.; Kupiainen-Maatta, O.; Praplan, A. P.; Adamov, A.; Amorim, A.; Bianchi, F.; Breitenlechner, M.; et al. Molecular Understanding of Sulphuric Acid-Amine Particle Nucleation in the Atmosphere. *Nature* **2013**, *502*, 359–363.
- (60) McMurry, P. H.; Stolzenburg, M. R. On the Sensitivity of Particle-Size to Relative-Humidity for Los-Angeles Aerosols. *Atmos. Environ.* **1989**, *23*, 497–507.
- (61) Liu, B. Y. H.; Pui, D. Y. H.; Whitby, K. T.; Kittelson, D. B.; Kousaka, Y.; McKenzie, R. L. Aerosol Mobility Chromatograph: New Detector for Sulfuric-Acid Aerosols. *Atmos. Environ.* **1978**, *12*, 99–104.
- (62) Zhao, J.; Eisele, F. L.; Titcombe, M.; Kuang, C. G.; McMurry, P. H. Chemical Ionization Mass Spectrometric Measurements of Atmospheric Neutral Clusters using the Cluster-CIMS. *J. Geophys. Res.: Atmos.* **2010**, *115*, D08205.
- (63) Smith, J. N.; Barsanti, K. C.; Friedli, H. R.; Ehn, M.; Kulmala, M.; Collins, D. R.; Scheckman, J. H.; Williams, B. J.; McMurry, P. H. Observations of Aminium Salts in Atmospheric Nanoparticles and Possible Climatic Implications. *Proc. Natl. Acad. Sci. U.S.A.* **2010**, *107*, 6634–6639.
- (64) Canagaratna, M. R.; Jayne, J. T.; Jimenez, J. L.; Allan, J. D.; Alfarra, M. R.; Zhang, Q.; Onasch, T. B.; Drewnick, F.; Coe, H.; Middlebrook, A.; et al. Chemical and Microphysical Characterization of Ambient Aerosols with the Aerodyne Aerosol Mass Spectrometer. *Mass Spectrom. Rev.* **2007**, *26*, 185–222.